Hindawi
Geofluids
Volume 2022, Article ID 1324531, 17 pages
https://doi.org/10.1155/2022/1324531

*Research Article*

# Large Eddy Simulation Research on the Evolution Mechanism of Aircraft Wake Influenced by Cubic Obstacle

**Weijun Pan, Yuming Luo, Shuai Han, and Hao Wang**

*Civil Aviation Flight University of China, Guanghan Sichuan Province 618307, China*

Correspondence should be addressed to Weijun Pan; wjpan@cafuc.edu.cn and Yuming Luo; 1149417522@qq.com

Received 21 March 2022; Revised 5 May 2022; Accepted 28 May 2022; Published 24 June 2022

Academic Editor: Hao Wu



Aircraft wake is a kind of intense air movement, and the study of its generation, development, and dissipation law is of great significance to the flight safety. There are abundant researches on the evolution of aircraft wakes affected by weather and ground effects; however, there are few studies on the influence of a single obstacle on the evolution of aircraft wake. In this article, in order to explore the influence of a single obstacle on the evolution of aircraft wake, firstly, we develop a computational fluid dynamics-based method of simulation of aircraft wake affected by cubic obstacle of different heights in order to obtain the wake intensity changes and position changes before and after being affected by the obstacle. Then, the result data are visualized and analyzed, and we obtain the results of velocity and $Q$ criterion contours, circulation, and data related to wake vortex structure. CFD simulations are conducted, including the cases of the vertical distance between wake vortex and obstacle which is 20 m, 60 m, 100 m, and no obstacle. The quantitative results indicate that a single obstacle also has a great influence on the evolution of the wake vortex. Obstacle will shorten the time for the wake vortex to enter the fast decay stage, and the smaller the distance the wake vortex is above the obstacle, the faster it enters the fast decay stage. In the same time, the circulation will reduce 20% more under the same calculation time when the wake is 20 m above the obstacle than when the wake is 100 m above the obstacle, and the circulation will reduce 45% more than when there is no obstacle. Single obstacle also leads to the generation of multiple secondary vortices and rotates around the wake vortex, resulting in the increase of wake vortex core radius, wake vortex core spacing, and wake vortex height.

## 1. Introduction

Aircraft wake separation is a key factor restricting the growth of airport runway throughput and the number of flights [1, 2], and it is also a key factor affecting flight safety [3]. In the 1960s, an F-104 suddenly flipped after encountering an enhanced wake generated by the tip of the right wing of the front plane, causing it to collide with the front plane and resulting in the crash of two planes. This is the first safety accident in the world caused by wake [4]. Researchers have been conducting a series of studies on the generation and evolution of aircraft wake. The early research was in 1970 [5], which studied the motion stability of a pair of cylindrical vortices in the extended near-field to mid-far-field range, using the first-order model of Biot-Savart law, using a pair of vortex filaments extending parallel to infinity with disturbing components to describe the stability of the wake vortex. In 1985 [6], the wake vortex estimation model is proposed for the first time, assuming that the wake per unit length pulse is related to viscous drag, buoyancy, and turbulence dissipation and then determining the circulation, velocity, and vertical position of the wake. Since then, the previous wake vortex estimation model has been improved by considering the effects of near-ground and lateral wind [7]. In further research [8], the factor of viscous drag in the wake vortex estimation model was excluded, and the empirical formula of turbulence dissipation was given by using the method of vortex dissipation rate instead of turbulence energy.

In the numerical study in 2003 [9], by considering factors such as wind, turbulence, stable stratification, and near the ground, a parametric wake transmission and dissipation model was proposed, and it was used as a function of aircraft and environmental parameters for real-time prediction of possible wakes. Some scholars [10] use the Reynolds average method to simulate the flow around the aircraft and study

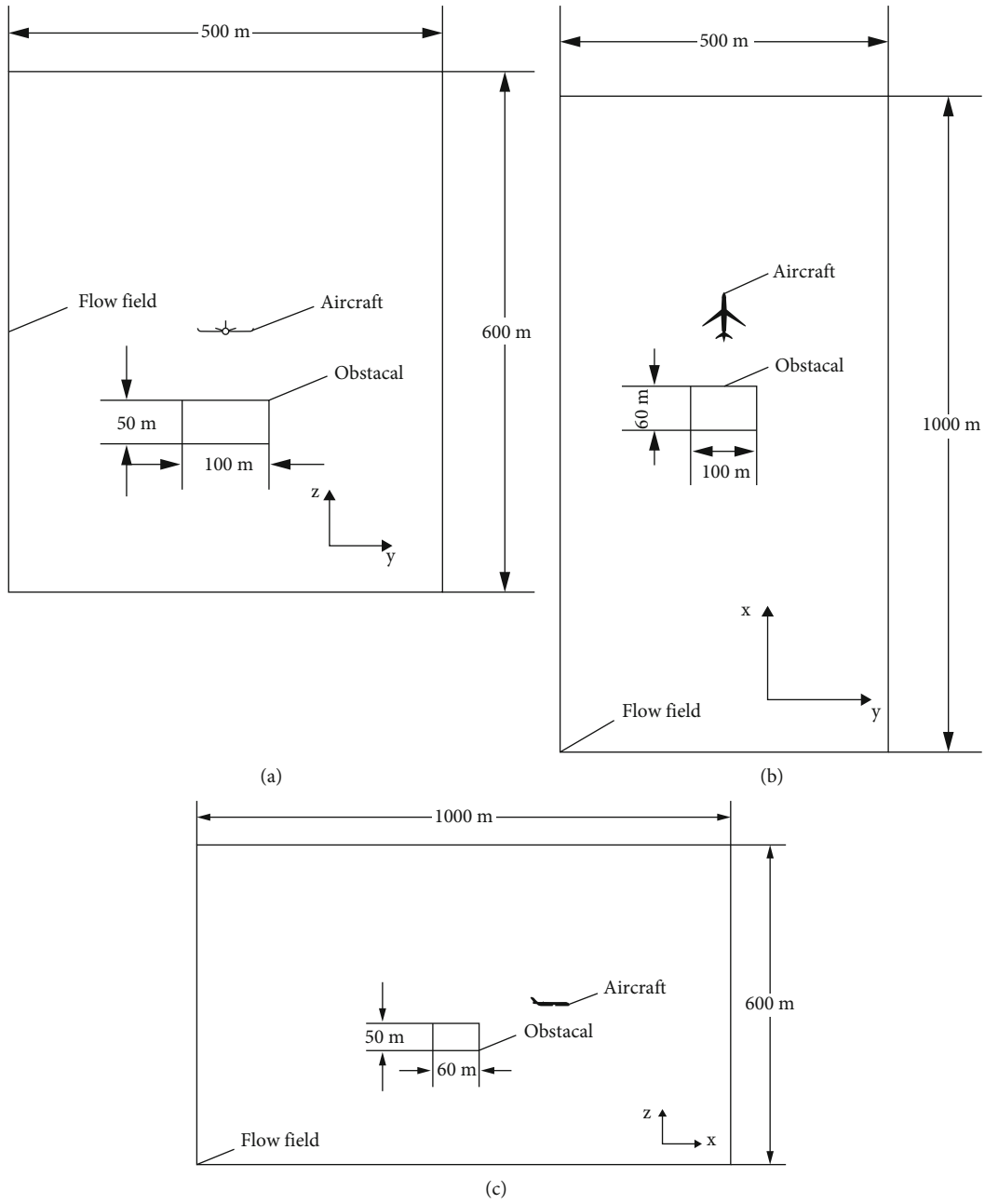


Figure 1: Three views of computational domain: (a) main view, (b) top view, and (c) left view.

the winding process of the wake vortex formation stage. Some scholars [11] initialize the wake vortex distribution with a constant velocity along the flight direction and study the interaction between the fully roll up wake vortex after initialization and the ground. This simplified landing phase modeling method has also been adopted by other researchers [12].

Since then, the researchers [13] conduct direct numerical simulations and large eddy simulations for the merging process of the wake vortex system and its instability. They believe that the merging of the wake vortex is caused by vorticity exchange and is affected by the viscous diffusion of the vortex center and relate to the critical ratio of the wake vortex diffusion radius and vortex pitch. Considering various atmospheric conditions such as turbulence, thermal stability, and wind shear [14], large eddy simulation methods are used to study the dynamic process of wake vortex generation and dissipation. In recent years, with the continuous development of the RANS-LES coupling method, researchers [15, 16] simulate the more realistic and complex wake structure in the near-ground phase and use this method to study the influence of crosswind and ground obstacles on the dissipation of the wake vortex. In 2016 [17], researchers established a numerical model of an independent trailing wake vortex and wall surface and simulated the interaction between the wake vortex and the ground with the help of direct numerical simulation methods and further explored the linear optimal initial disturbance problem. Other researchers [18] use

large eddy simulation methods to explore the influence of crosswind and atmospheric turbulence on wake vortex dissipation. The results proved that low-speed crosswind and low turbulence have relatively weak influence on wake vortex dissipation, while strong side wind can effectively accelerate the occurrence of wake vortex dissipation behavior. Researchers [19] compare the tangential velocity distribution of the wake vortex with the classical wake vortex model, and the results showed that the tangential velocity profile of the wake vortex in the numerical simulation results is in good agreement with different wake vortex models.

Chinese scholars [20] discuss the evolution and dissipation process of the approach area wake vortex and its influence on aerodynamic forces. The results indicate that the Mach number has an effect on the flow direction vorticity and the "kink" phenomenon at the main vortex and the secondary vortex center, but has little effect on the flow direction and the fusion position of the main vortex and the secondary vortex center; the Reynolds number only affects the flow direction vorticity, the dimensionless flow direction speed, and the "kink" phenomenon at the main vortex center and the secondary vortex center, but has no effect on the flow direction speed and the fusion position at the secondary vortex center. Researchers [21] use adaptive grid technology in the large eddy simulation test of aircraft wake vortex evolution, which significantly reduced the number of grids and improved the computational efficiency of numerical simulation. At the same time, they also proposed the generation of wake vortex on lift surface. The method is used to study the evolution characteristics of the aircraft wake vortex in the atmosphere. Other researchers [22] use large eddy simulation based on adaptive grids and study three different environmental turbulence intensities. Numerical results show that the refined grid in the wake region generated by the adaptive grid method can capture wake vortices more effectively. Through numerical simulation, they [23] also find that uniform crosswind convection and linear vertical shear crosswind convection will also affect the vortex intensity. This effect is inversely proportional to the cube of the vortex interval, so the effect is more obvious on smaller separation vortex pairs.

The contributions to this article is as follows. First, a CFD-based simulation method for the influence of a single obstacle on the evolution of the aircraft wake is developed, and the wake intensity and wake position change data are obtained at different conditions. It includes the calculation scheme of the aircraft wake field and the realization method of numerical simulation of wake affected by obstacle. Then, in order to analyze the intensity change and position change of the aircraft wake affected by obstacle, we obtained the velocity and $Q$ criterion contours, circulation, wake vortex height, and other variables. LES method is used to realize the numerical simulation of the wake field. Our present work is aimed at quickly understanding the evolution of aircraft wake in various scenarios from the perspective of engineering application. It can be used to optimize aircraft wake separation and improve flight safety. The study of wake affected by a single obstacle is different from the study of wake affected by weather and ground effect. The obtained wake intensity and position changes are also useful for understanding the evolution of wakes in different scenarios.

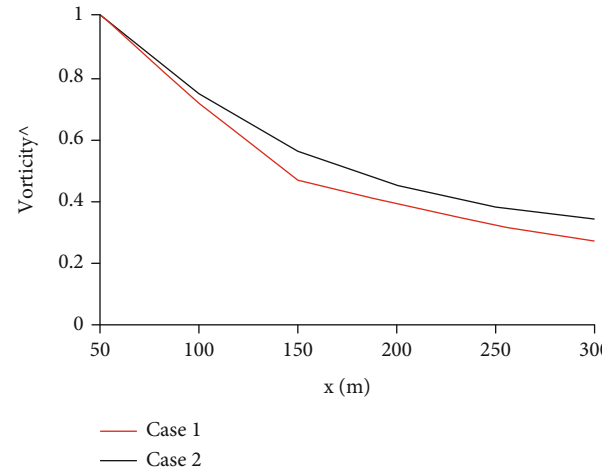


Figure 2: Vorticity curves at different positions when only the wing is retained and when the entire aircraft is retained.

## 2. Model Building

*2.1. Governing Equations.* According to the vortex theory of turbulence, large-scale vortices are the main cause of turbulent pulsation and mixing. Large-scale vortices obtain energy from the main flow of the flow field. They are highly nonisotropic and vary with the flow situation. Large-scale vortices transfer energy to small-scale vortices through interaction. Small-scale vortices mainly dissipate energy in the flow field. They are almost isotropic, and the small-scale vortices in different flows have many commonalities. The above recognition has led to the numerical solution of large-scale eddy simulation, namely, large eddy simulation. This method uses the unsteady filtered Navier-Stokes equations to directly solve the large-scale vortices and uses the subgrid stress model to approximate the influence of small vortices on large vortices. The LES contains different subgrid-scale models. According to our previous calculation experience and engineering practice, we choose the WALE-LES model, which is suitable for solving the problem of three-dimensional wake field, and the calculation time and resource requirements are also suitable. The filtered N-S equations are as follows:

$$\frac{\partial \rho}{\partial t} + \frac{\partial}{\partial x_i}(\rho \overline{u_i}) = 0, \tag{1}$$

$$\frac{\partial}{\partial t}(\rho \overline{u_i}) + \frac{\partial}{\partial x_i}\left(\rho \overline{u_i u_j}\right) = \frac{\partial}{\partial x_j}\left\{\left[\mu\left(\frac{\partial \overline{u_i}}{\partial x_j} + \frac{\partial \overline{u_j}}{\partial x_i}\right)\right] - \frac{2}{3}\mu \frac{\partial \overline{u_l}}{\partial x_l}\delta_{ij}\right\} - \frac{\partial \bar{p}}{\partial x_i} - \frac{\partial \tau_{ij}}{\partial x_j}, \tag{2}$$

$$\frac{\partial \rho \overline{h_s}}{\partial t} + \frac{\partial \rho \overline{u_i} \overline{h_s}}{\partial x_i} - \frac{\partial \bar{p}}{\partial t} - \overline{u_j}\frac{\partial \bar{p}}{\partial x_i} - \frac{\partial}{\partial x_i}\left(\lambda \frac{\partial \bar{T}}{\partial x_i}\right) = -\frac{\partial}{\partial x_j}\left[-\frac{\mu_{\mathrm{SGS}} C_p}{\mathrm{Pr}_{\mathrm{SGS}}}\frac{\partial \bar{T}}{\partial x_j}\frac{1}{\text{subgrid enthalpy flux}}\right], \tag{3}$$

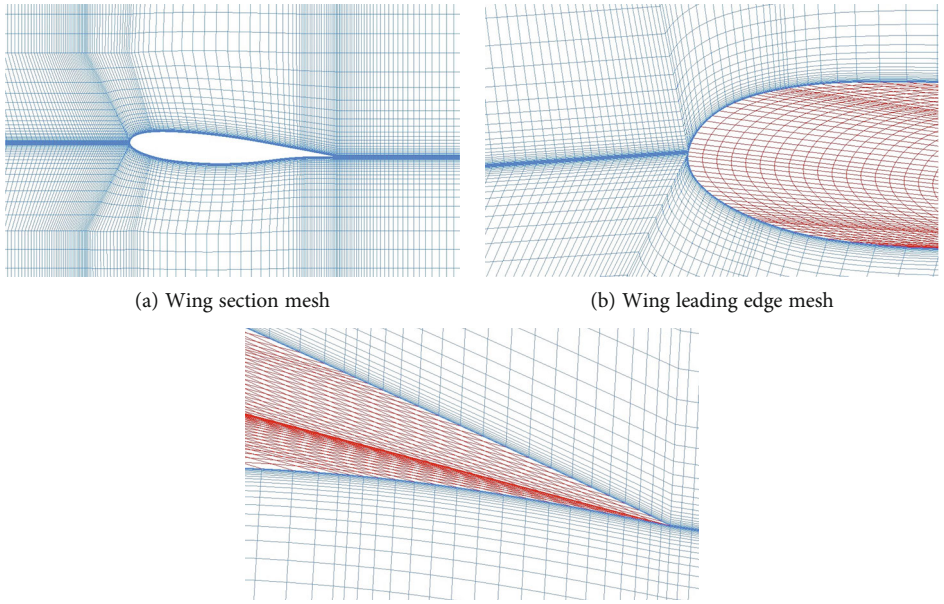

(a) Wing section mesh

(b) Wing leading edge mesh

(c) Wing trailing edge mesh

Figure 3: A330-200 wing computational mesh partial view.

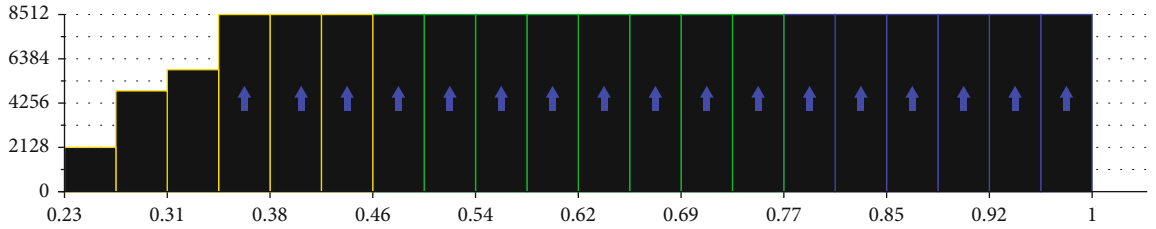


Figure 4: Mesh quality.

Table 1: Air and calculation parameter settings.

| Parameter | Value |
|---|---|
| Mach number | 0.29 |
| Pressure | 101.325 kPa |
| Temperature | 300 K |
| Flow courant number | 1 |
| Initial time step size | $1e-4(s)$ |
| Maximum time step size | $1e-3(s)$ |
| Minimum time step size | $1e-5(s)$ |
| Max iterations/time step | 20 |

where $\rho$ is the fluid density; t is time; $\overline{u_i}$, $\overline{u_j}$, and $\overline{u_l}$ are the three filtered velocity components; $x_i$, $x_j$, and $x_l$ are the three coordinate directions; $\bar{p}$ is the filtered pressure; $\mu$ is the fluid viscosity coefficient; $\delta_{ij}$ is the subgrid-scale strain rate; $\tau_{ij}$ is the subgrid-scale stress; $\overline{h_s}$ is the filtered sensible enthalpy; $\lambda$ represents the thermal conductivity; $\bar{T}$ is the filtered temperature; $\mu_{SGS}$ is the subgrid viscosity; $Pr_{SGS}$ is a subgrid Prandtl number equal to 0.85; $C_p$ is the specific heat.

Equations (1)–(3) are the filtered Navier-Stokes equations. Through these equations, we can effectively filter out the vortices whose scales are smaller than the filter width or grid spacing used in the computations. Through Equations (1)–(3), we can realize the simulation of large-scale vortices.

$$\tau_{ij} - \frac{1}{3}\tau_{kk}\delta_{ij} = -\mu_t\left(\frac{\partial\overline{u_i}}{\partial x_j} + \frac{\partial\overline{u_j}}{\partial x_i}\right), \tag{4}$$

where $\tau_{kk}$ represents the isotropic part of the subgrid-scale stresses; $\mu_t$ is the subgrid-scale turbulent viscosity.

Equation (4) is the subgrid turbulence model, it can calculate the influence of the small vortex on the large vortex, and this is one of the most important aspects of large eddy simulation.

$$\mu_t = \rho L_s^2 \frac{\left(S_{ij}^d S_{ij}^d\right)^{3/2}}{\left(\overline{S_{ij}S_{ij}}\right)^{5/2} + \left(S_{ij}^d S_{ij}^d\right)^{5/4}}, \tag{5}$$

$$L_s = \min\left(kd, C_w V^{1/3}\right), \tag{6}$$

Table 2: Calculation results of different mesh numbers.

| Number of mesh (ten thousand) | Vorticity (1/s) | Percentage change | $Q$ criterion ($s^{-2}$) | Percentage change | Minimum mesh size of wake area (m) |
|---|---|---|---|---|---|
| 1432 | 4.183 | | 10.108 | | 1 |
| 2058 | 4.452 | 6.43% | 10.535 | 4.05% | 0.8 |
| 2521 | 4.615 | 3.66% | 10.716 | 1.72% | 0.6 |
| 3078 | 4.871 | 5.55% | 10.839 | 1.15% | 0.5 |
| 3479 | 5.026 | 3.18% | 11.028 | 1.74% | 0.4 |
| 4019 | 5.152 | 2.51% | 11.157 | 1.17% | 0.3 |
| 4679 | 5.180 | 0.54% | 11.212 | 0.49% | 0.2 |
| 5156 | 5.203 | 0.44% | 11.257 | 0.40% | 0.1 |

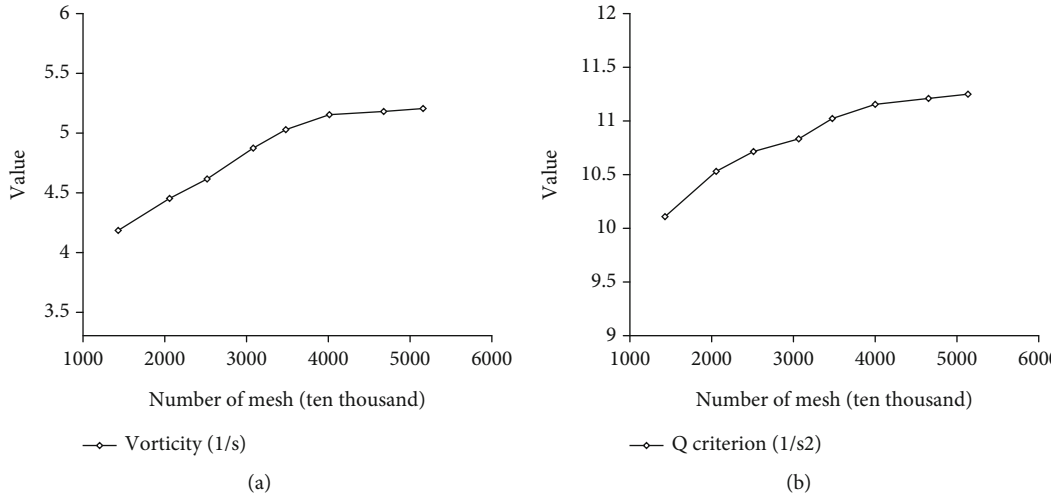


Figure 5: Mesh independence verification results.

$$S_{ij}^{d} = \frac{1}{2}\left(\overline{g}_{ij}^{2} + \overline{g}_{ji}^{2}\right) - \frac{1}{3}\delta_{ij}\overline{g}_{kk}^{2}, \overline{g}_{ij} = \frac{\partial \overline{u}_i}{\partial x_j}, \quad (7)$$

where $L_s$ is the mixing length for subgrid scales; $\overline{S_{ij}}$ is the rate-of-strain tensor for the resolved scale; $k = 0.41$ is the von Karman constant; d is the distance to the closest wall; $C_w = 0.325$ is a constant; $V$ is the volume of a computational cell.

Equations (5) and (6) are used to calculate the subgrid-scale turbulent viscosity. The subgrid-scale model is based on eddy viscosity; that is, the influence caused by turbulence pulsation is described by the turbulence viscosity coefficient, that is, eddy viscosity. Therefore, the calculation of small vortices can be realized by Equations (4)–(7).

*2.2. Physical Models.* The aircraft model used in this article is A330-200, the aircraft's wingspan is 60 m, fuselage length is 59 m, and the tail height is 17 m. The aircraft model in this paper only retains the original wing and omits the fuselage and tail, mainly to reduce the number of mesh and improve computational efficiency. The model geometry processing and flow field division are carried out in the ANSYS DM module. The fluid domain is a rectangular parallelepiped with length, width, and height of 1000 m × 500 m × 600 m; the $x$-axis is the flight direction of aircraft and is 1000 m long; the $y$-axis is the left and right direction of the wingspan of the aircraft, and the length is 500 m; the $z$-axis is the vertical direction of the aircraft, and the length is 600 m. Obstacle is simulated by setting walls at different positions at the flow field. This article chooses three vertical distances which

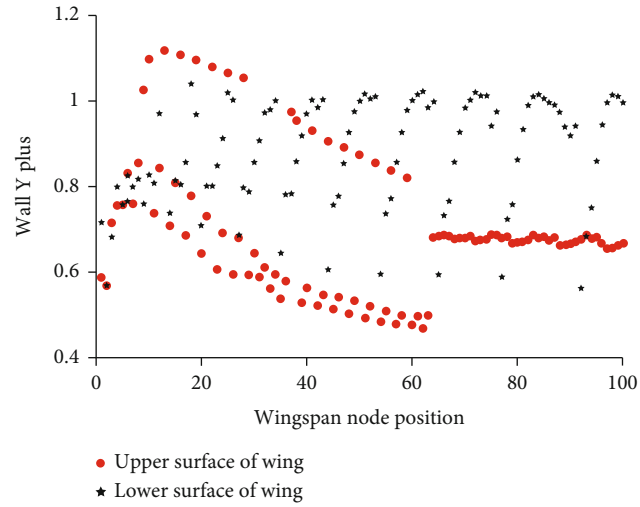


Figure 6: $Y$ plus value of the wing surface.

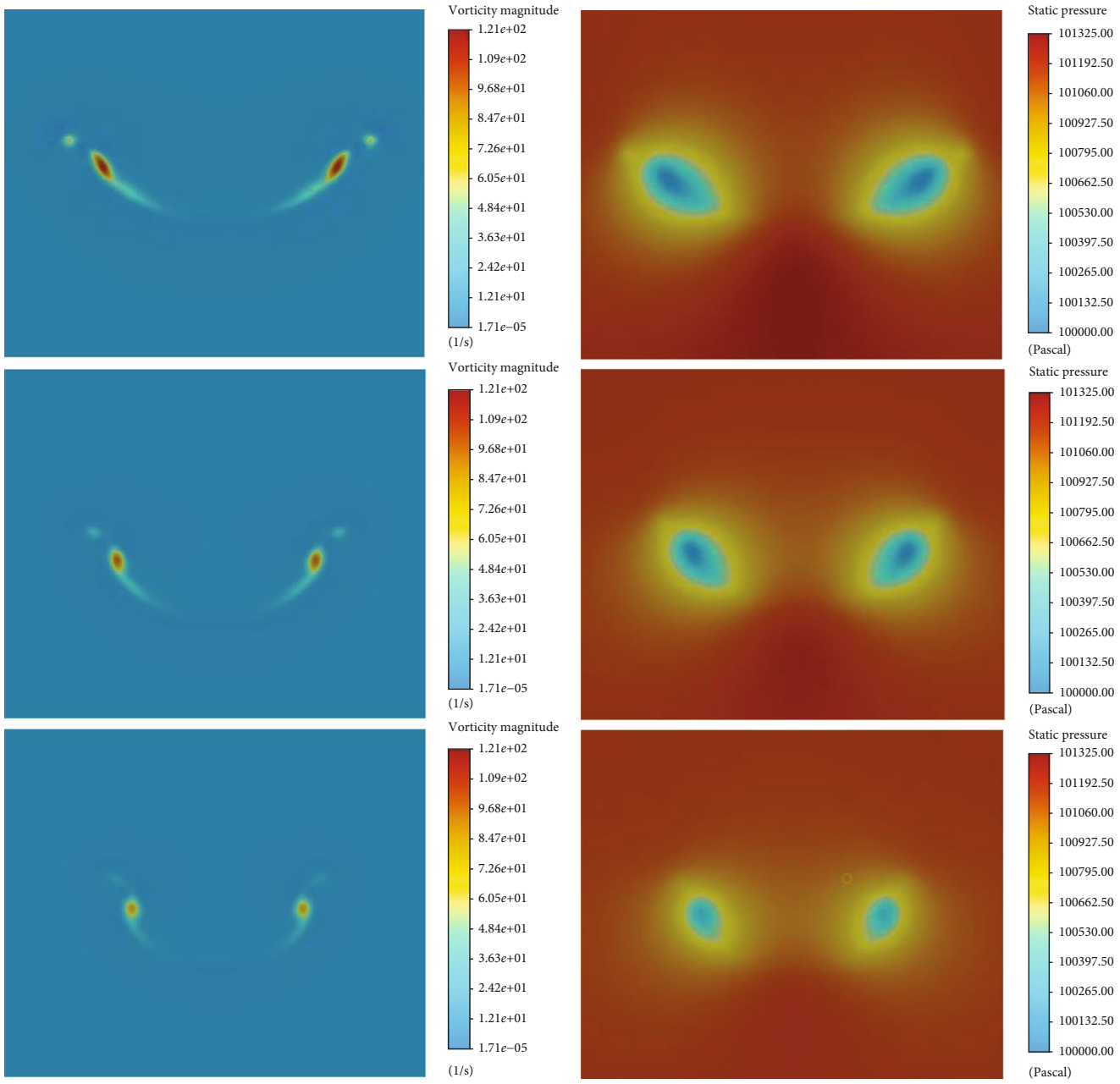


Figure 7: The development of wing tip vortices: (a) vorticity contour and (b) pressure contour.

are 20 m, 60 m, and 100 m above the obstacle. The obstacle set in this article is a cuboid obstacle similar to a tall building or a mountain top. The width of the obstacle is about 100 m, and the front and back length of the obstacle is about 60 m. Figure 1 is the three views of the physical model. The figure shows a schematic diagram of the relative position of the aircraft and the obstacle. Figure 2 shows the comparison between the calculation results when only the wings are retained and the calculation results of the whole aircraft. It can be seen that when the whole aircraft is used for calculation, which is case 1, the vorticity will be 5% smaller than the calculation result of leaving only the wing, which is case 2, but the law of vorticity change is basically the same. So in our opinion, it is acceptable to keep only the wings for computation while reducing the number of mesh and speeding up the computation considerably.

*2.3. Mesh Models.* In order to get high-quality mesh, we adopt a structured meshing method based on the finite volume method. In this article, the inlet of the flow field, the surface of the aircraft, the wake area, and the outlet of the flow field are all locally encrypted. The number of structured mesh is about 52 million, the global mesh quality is above 0.23, and there are 12,000 mesh below 0.35. The height of the first layer of mesh cell near the aircraft wall is $5.3e-6$

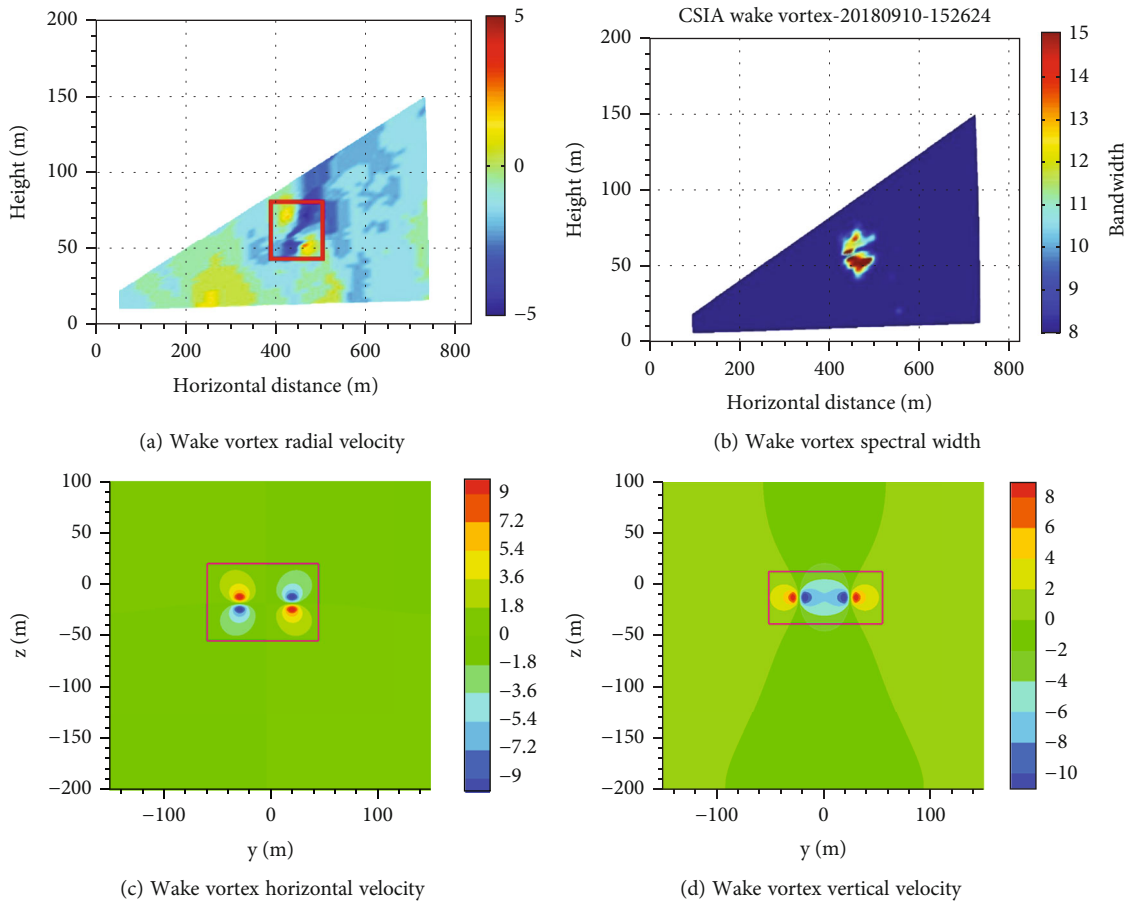


(a) Wake vortex radial velocity

(b) Wake vortex spectral width

(c) Wake vortex horizontal velocity

(d) Wake vortex vertical velocity

Figure 8: Comparison of the initial state of the wake vortex between radar detection and numerical simulation results.

m and ensure that $Y+$ is near 1, the number of mesh layers in the boundary layer is 40, and the minimum grid size of the wake area is 0.1 m. The above is the mesh model selected for the final calculation after completing the mesh independence test. During the mesh independence verification, the mesh densification area did not change, but the mesh size was changed to obtain different orders of magnitude mesh models. The mesh independence verification results are given in the simulation results. Figure 3 shows the local mesh and mesh quality. The yoz profile mesh can see the overall encryption of the area where the aircraft is located. The wing profile mesh can see the boundary layer area on the wing surface. Figure 4 shows the $Y+$ value of the wing surface.

*2.4. Boundary Condition Setting.* In this article, the cuboid computational domain is used in the calculation of different cases. The boundary in the calculation includes the six faces of the rectangular parallelepiped calculation domain, the entire wall of the aircraft, and the entire wall of the obstacle. Among them, the boundary condition of the six faces of the cuboid calculation domain is the pressure far field, the boundary condition of the aircraft wall is a stationary wall, and the boundary condition of the obstacle wall is a moving wall; and its speed is the same as the air velocity in the flow field. This article mainly studies the evolution of wakes under different vertical distances from obstacles. We choose three vertical heights, which are 20 m, 60 m, and 100 m from the obstacle, and study the dissipation law of the wake in these three cases and compare the results with the no obstacle results.

In the calculation of this article, the ideal gas is selected for the fluid in the flow field, and the angle between the gas and the aircraft is 5°. The specific parameters of the gas are shown in Table 1. Solving method selection, pressure-velocity coupling choose PISO method, in space discretization method, least squares cell-based method is used for gradient, second order is used for pressure, second order upwind is used for momentum and energy, and the transient formula is bounded second order implicit. The type selection in time advancement is adaptive and CFL-based.

## 3. Calculation Results

*3.1. Grid Independence Verification.* According to the calculation principle of large eddy simulation, vortices smaller than the smallest mesh cell in the computational domain will be filtered, so the mesh size of the wake vortex area has a great influence on the accuracy of the calculation results. We calculate eight groups of different numbers of mesh cells to complete the mesh independence test. Table 2 shows all the calculation mesh and the calculation results.

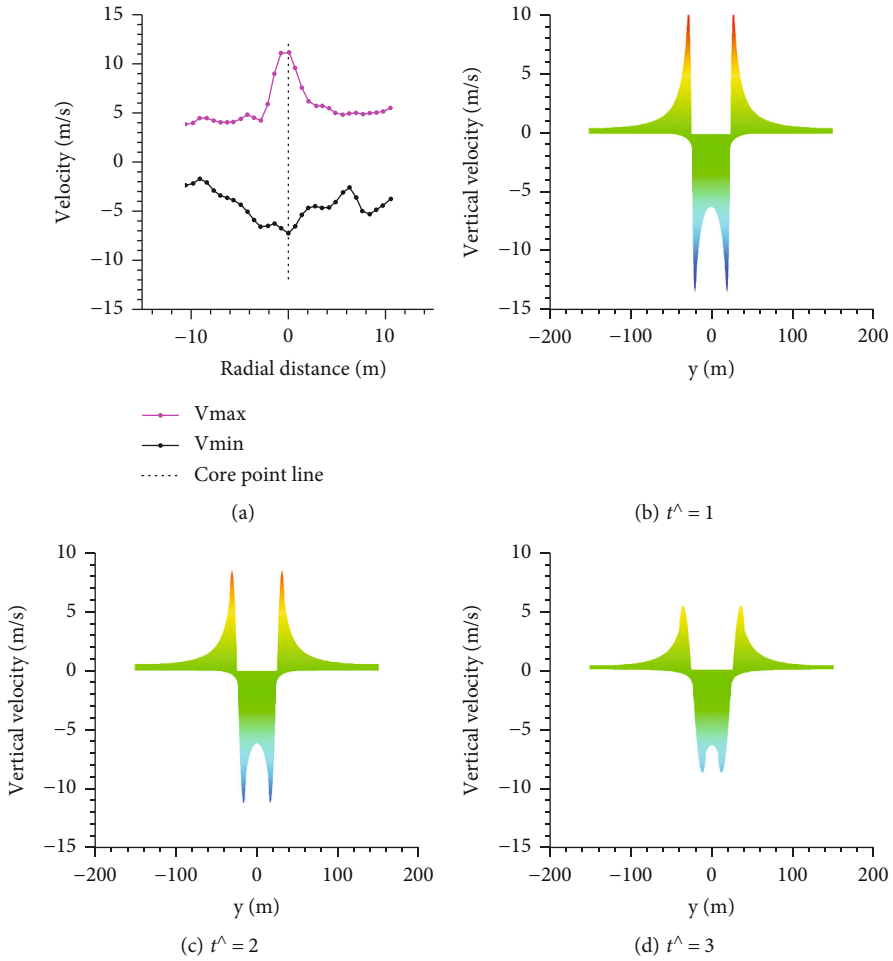


Figure 9: Wake vortex velocity distribution: (a) radar measurement result and (b–d) numerical simulation results.

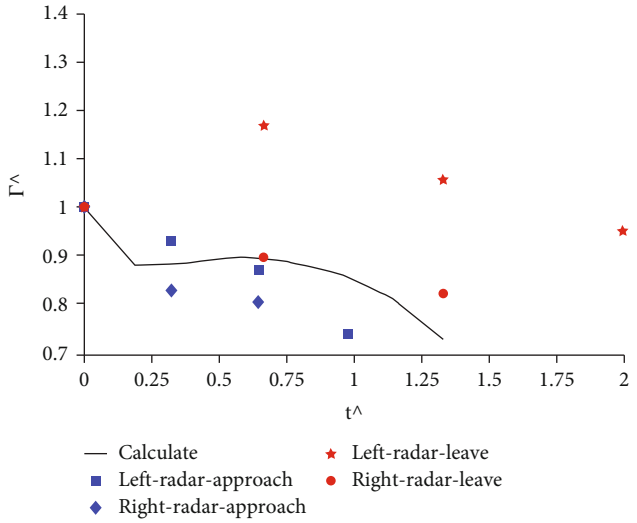


Figure 10: Comparison of wake vortex circulation attenuation between radar detection and numerical simulation results.

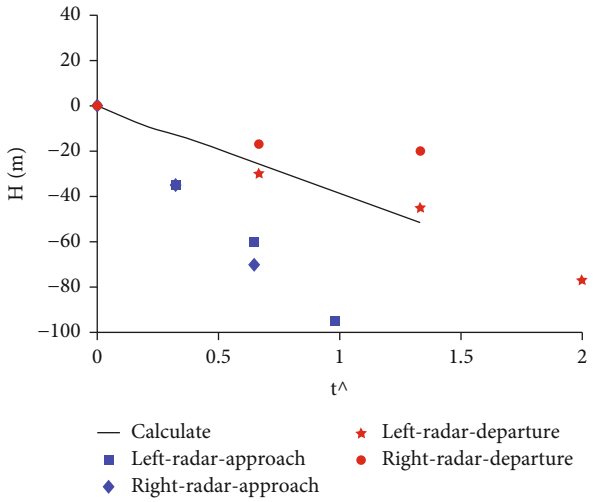


Figure 11: Comparison of wake vortex height variation between radar detection and numerical simulation results.

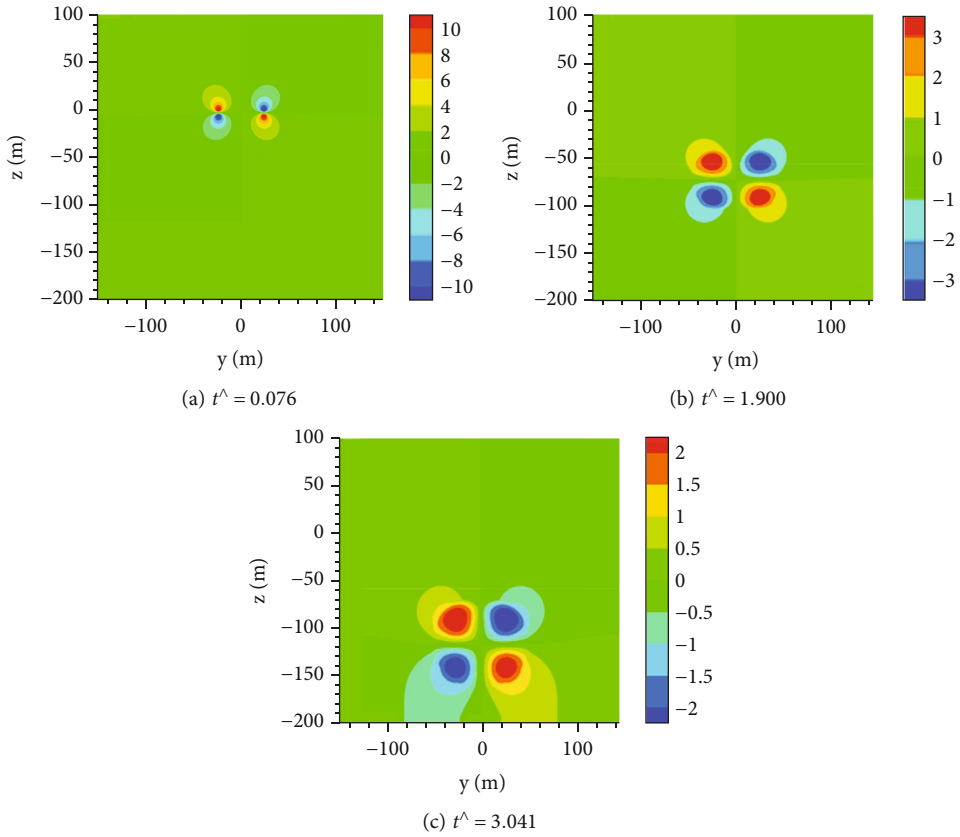


FIGURE 12: Contours of $y$ velocity at different times when there is no obstacle.

The calculation of the percentage of change is shown in

$$\text{Percentage change} = \frac{A_{i+1} - A_i}{A_i}, \tag{8}$$

where $A_{i+1}$ and $A_i$ are the calculation results of two adjacent numbers of mesh cells, $A_{i+1}$ is the one with the larger number of mesh cell, and $A_i$ is the one with the smaller number of mesh cell. Figure 5 shows the curves of physical quantity changing with the number of mesh cells.

The result of the vorticity and $Q$ criterion obtained here is the maximum value at $x = -600$ in the calculation domain, which is the maximum value at 600 meters behind the obstacle. Through postprocessing, it can be found that in the computational domain, the vorticity and the $Q$ criterion at the vortex center are the largest, so we use the maximum physical quantity to reflect the strength of the wake vortex to the corresponding stage. It can be seen from the results that when the number of mesh cell is about 52 million, the changes in vorticity and $Q$ criterion are already very small. At the same time, considering computing time and computing resources, we select 52 million mesh cells to complete the calculations in this article. The $Y$ plus value of the upper and lower surfaces of the wing as shown in Figure 6 is basically around 1, which shows that the wing boundary layer mesh used in this paper meets the requirements of the large eddy simulation calculation for the boundary layer mesh.

In this paper, the vorticity contours at different positions along the flow direction are also intercepted, as shown in Figure 7. It can be seen that the part with strong vorticity in the same section is the wake vortex core, and the initial vorticity can reach more than $100\,s^{-1}$. The region farther from the vortex core corresponds to the weaker vortex intensity. This is because the airflow velocity in the vortex core region is large, and correspondingly, the static pressure in the vortex core region is relatively small, which can also be seen from the pressure contours on the right. Comparing the vorticity contours of different sections, it can be seen that with the development of the vortex, the wake vortex gradually rolls up, the vorticity gradually becomes smaller, the shear layer of the trailing edge of the wing gradually dissipates, and its vorticity is involved in the main vortex, which is consistent with the actual situation. Therefore, the computational mesh used in this paper can accurately capture the wake vortex.

*3.2. Comparison of Numerical Simulation Results and Radar Detection Data.* In order to further verify the reliability of the numerical simulation results, the numerical simulation calculation results and the radar detection results are compared and analyzed in this paper. Figures 8(a) and 8(b) show the visualization of the wake vortex velocity and spectral width detected by the radar; Figures 8(c) and 8(d) show the numerically simulated aircraft wake vortex velocity contours. It can be seen that both the numerical simulation

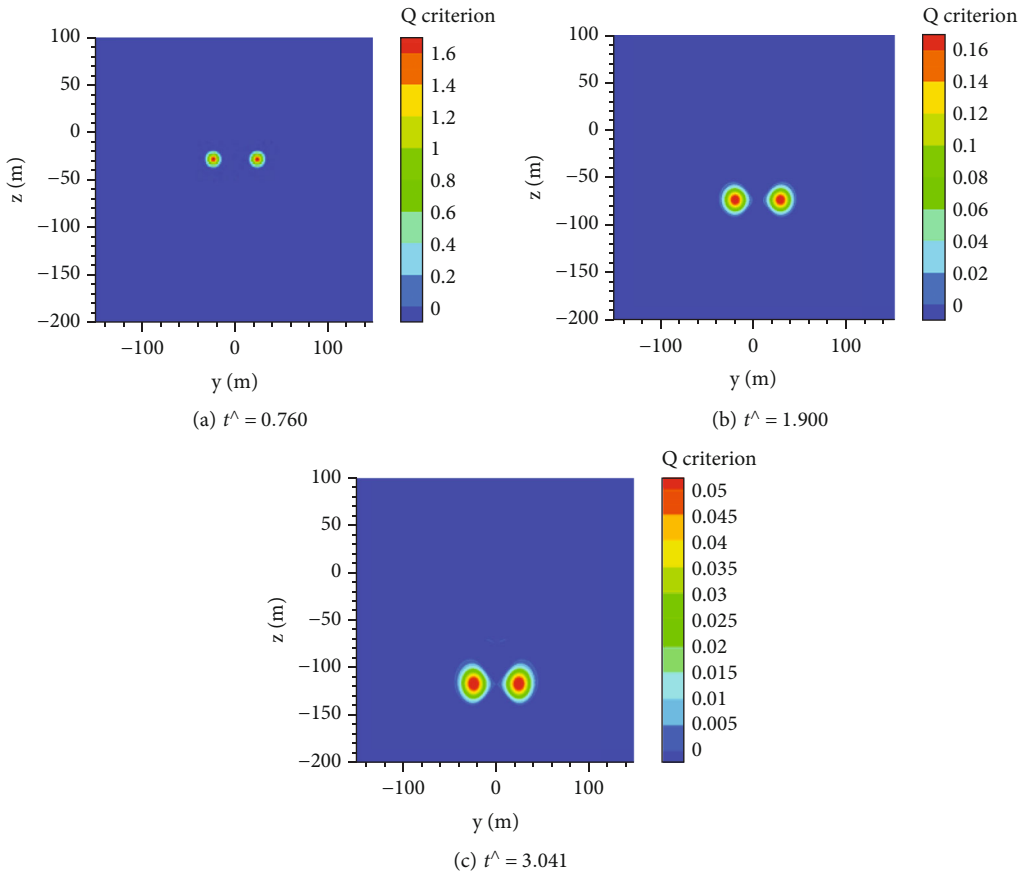


Figure 13: Contours of $Q$ criterion at different times when there is no obstacle.

results and the radar detection results show two opposite velocity pairs of the wake vortex, and the velocity is relatively close. This shows that the wake vortex velocity field obtained by numerical simulation is similar in structure to the wake vortex velocity field directly obtained by radar detection.

Figure 9 shows the velocity distribution near the wake vortex core obtained by radar detection and numerical simulation. By comparison, it can be found that both the radar detection results and the numerical simulation results have the largest velocity near wake vortex core, while the velocity gradually decreases away from wake vortex core. This shows that the wake vortex velocity distribution obtained by numerical simulation is similar to that of radar detection. Of course, because there is a background wind field during radar detection, its velocity distribution fluctuates to a certain extent.

Figures 10 and 11 are the results of the wake vortex circulation and the wake vortex height obtained by radar detection and numerical simulation. In the numerical simulation, the variation of the left and right vortex circulation and height is basically symmetrical, so only single vortex results are given. The radar detection data given here is obtained by screening a large number of radar detection data and excluding the situation with a large background wind field as much as possible. Limited by the radar scan period and scan angle, we generally only get three to four data for the wake vortex of an aircraft, because after a period of time, the aircraft wake vortex drifts out of the radar scanning angle.

Based on a set of approach data and a set of departure data of A330-200 aircraft, the circulation, wake vortex core radius, wake vortex core spacing, and time are all dimensionless. $\Gamma\wedge$ is the ratio of the circulation value at a certain time to the circulation value at the initial time, $b\wedge$ is the ratio of wake vortex core spacing at a certain time to the value at the initial time, $H$ is the wake vortex height, and $t\wedge$ is the ratio of the time to the characteristic time of the wake vortex.

It can be seen from the figure that the circulation results obtained by numerical simulation are close to the results of the left and right vortex circulation detected by the radar during the approach phase and are close to the results of the right vortex circulation during the departure phase. And it is consistent with the initial decay and rapid decay stage theory of the wake vortex circulation. This shows that the numerical simulation method can accurately calculate the decay of the wake vortex circulation. The variation of the left vortex circulation detected by the radar at the departure stage first increases and then decreases, which is mainly due to the error of the circulation estimation caused by the complex background wind field. In the variation results of the wake vortex height, the radar detection results in the approach phase and the

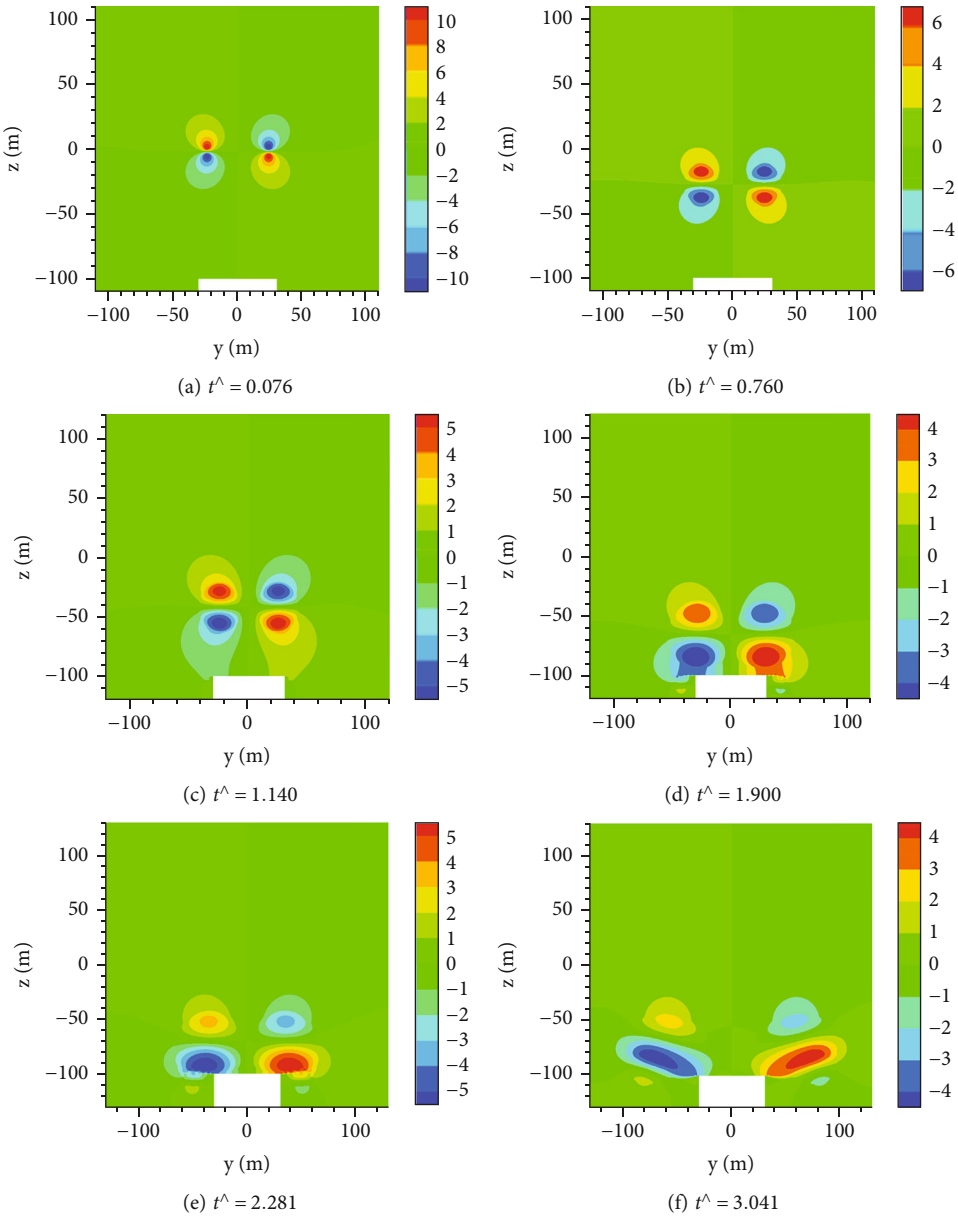


Figure 14: Contours of $y$ velocity at different times when the wake is 100 m above the obstacle.

left vortex detection results in the departure phase both show a rapid linear decline, which is consistent with the numerical simulation results. In the departure stage, the right vortex declines slowly, mainly due to the influence of the background wind field. By comparing the radar detection results and the numerical simulation results, we can confirm that the numerical simulation method used in this paper is reliable and can accurately calculate wake vortex intensity and position.

*3.3. Result Analysis.* In the analysis of the results, we gave the $Q$ criterion contours of the wake vortex at different times when there is obstacle and no obstacle. $Q$ criterion is a commonly used quantity that can be used to accurately identify vortices. We give the calculation method of the $Q$ criterion, such as Equations (9)–(11). We also obtained the results of the variation of the wake vortex circulation with time under different conditions. In this paper, we use the same circulation calculation method as in Holzäpfel's paper [10]. The calculation equation is shown as Equation (13). This method uses the average value of the circulation of 11 circles with a radius of 5 m-15 m from the center of the wake vortex core. At the same time, we also give the variation of wake vortex height and wake vortex core radius under different conditions and systematically analyze the influence of obstacle on the variation of wake vortex strength, structure, and position.

$$\Omega_{ij} = \frac{1}{2}\left(\frac{\partial u_i}{\partial x_j} - \frac{\partial u_j}{\partial x_i}\right), \tag{9}$$

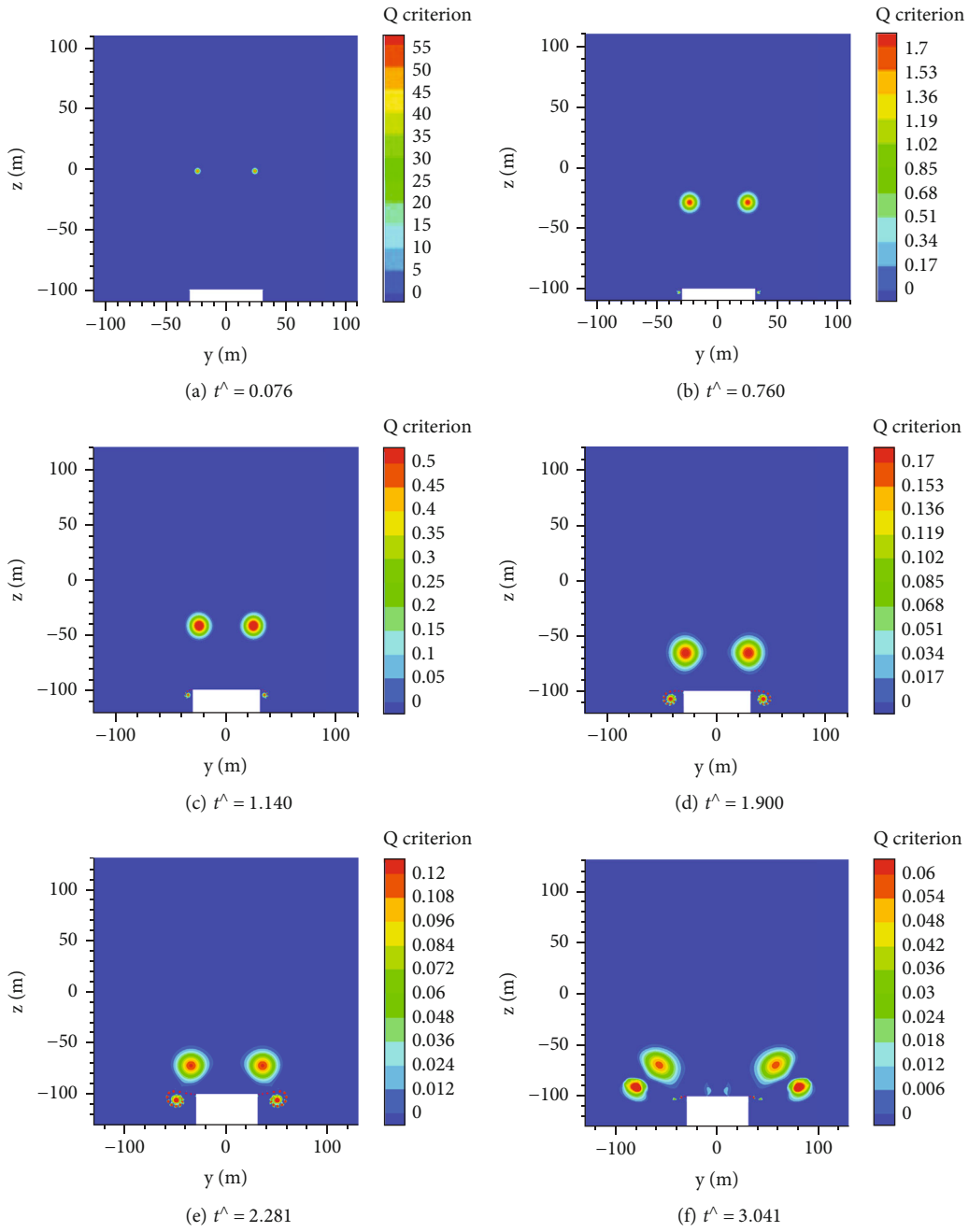


Figure 15: Contours of $Q$ criterion at different times when the wake is 100 m above the obstacle.

$$S_{ij} = \frac{1}{2}\left(\frac{\partial u_j}{\partial x_i} + \frac{\partial u_i}{\partial x_j}\right), \tag{10}$$

$$Q = \frac{1}{2}\left(\left\|S^2\right\| - \left\|\Omega^2\right\|\right), \tag{11}$$

$$\Omega^2 + S^2, \tag{12}$$

$$\Gamma_{5-15} = \frac{1}{11}\sum_{i=5}^{15}\Gamma_i, \tag{13}$$

where $\Omega_{ij}$ is the vorticity magnitude, $S_{ij}$ is the strain rate tensor, and $Q$ is the $Q$ criterion.

Figures 12 and 13 are the contours of the wake vortex velocity and the $Q$ criterion when there is no obstacle. The rotation velocity is one of the signs of the existence of the wake vortex, and the change of the velocity contours can reflect the change of the wake vortex shape to a certain extent. We can see that under the condition of no obstacle, the shape of the wake vortex does not change greatly. With the development of time, wake vortex core radius and wake vortex core spacing gradually increase. When there is no obstacle, the wake vortex structure is mainly affected by atmospheric turbulence and interaction of left and right vortices. Under the influence of atmospheric turbulence, wake vortex intensity and rotational velocity decrease. In the

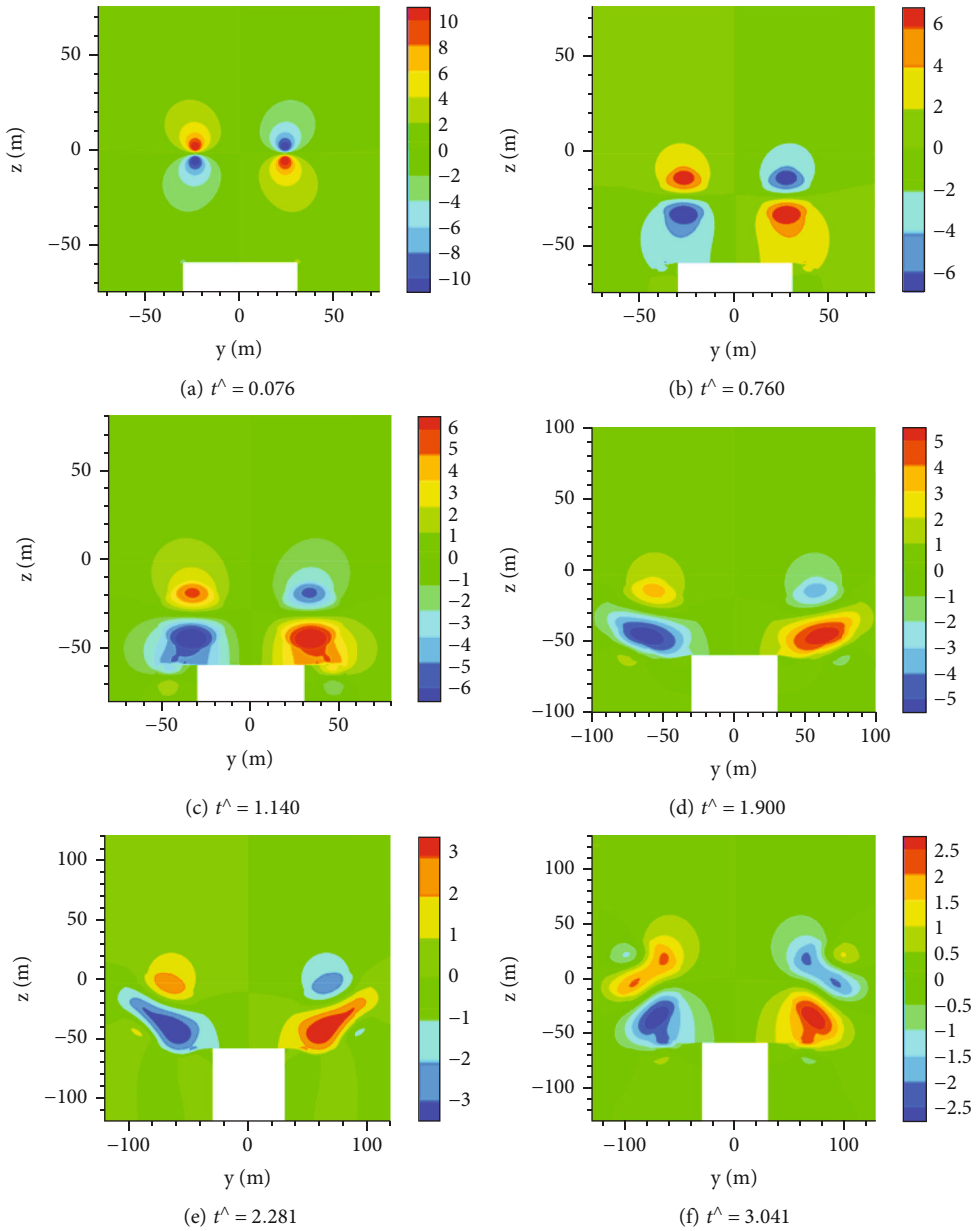


Figure 16: Contours of $y$ velocity at different times when the wake is 60 m above the obstacle.

initial stage of decay, wake vortex is mainly radial diffusion; that is, the wake vortex core radius increases continuously, and the interaction between the left and right vortices is still relatively small, and the increase of wake vortex core spacing is not obvious. As the wake vortex core radius increases, the interaction of the left and right vortices is enhanced and wake vortex core spacing increases faster than the initial stage. From the velocity contours, we can see that the velocities in the middle of the left and right vortices begin to affect each other, making the velocity cloud an irregular ellipse. From the $Q$ criterion contours, it can be found that the left and right vortices will gradually contact and connect. In general, when there is no obstacle, the wake vortex structure is mainly affected by turbulence and self-interaction.

Figures 14 and 15 are the contours of the wake vortex velocity and the $Q$ criterion when the wake is 100 m above the obstacle. By comparing the results with when there is no obstacle, we found that in the early stage of the calculation, that is, before $t^{\wedge} = 0.760$, the change of the wake vortex structure is basically the same as that in Figures 12 and 13. However, as the wake vortex height decreases, the structure of the wake vortex begins to be affected by the obstacle. What we found interesting is that the wake vortex velocity first changes at the edge of the obstacle, and the direction of the wake vortex velocity even reverses due to the obstruction of the obstacle. At this time, a secondary vortex opposite to the direction of rotation of the wake vortex is generated. After $t^{\wedge} = 2.281$, we can see from the $Q$ criterion contours that multiple secondary vortices are generated on both sides

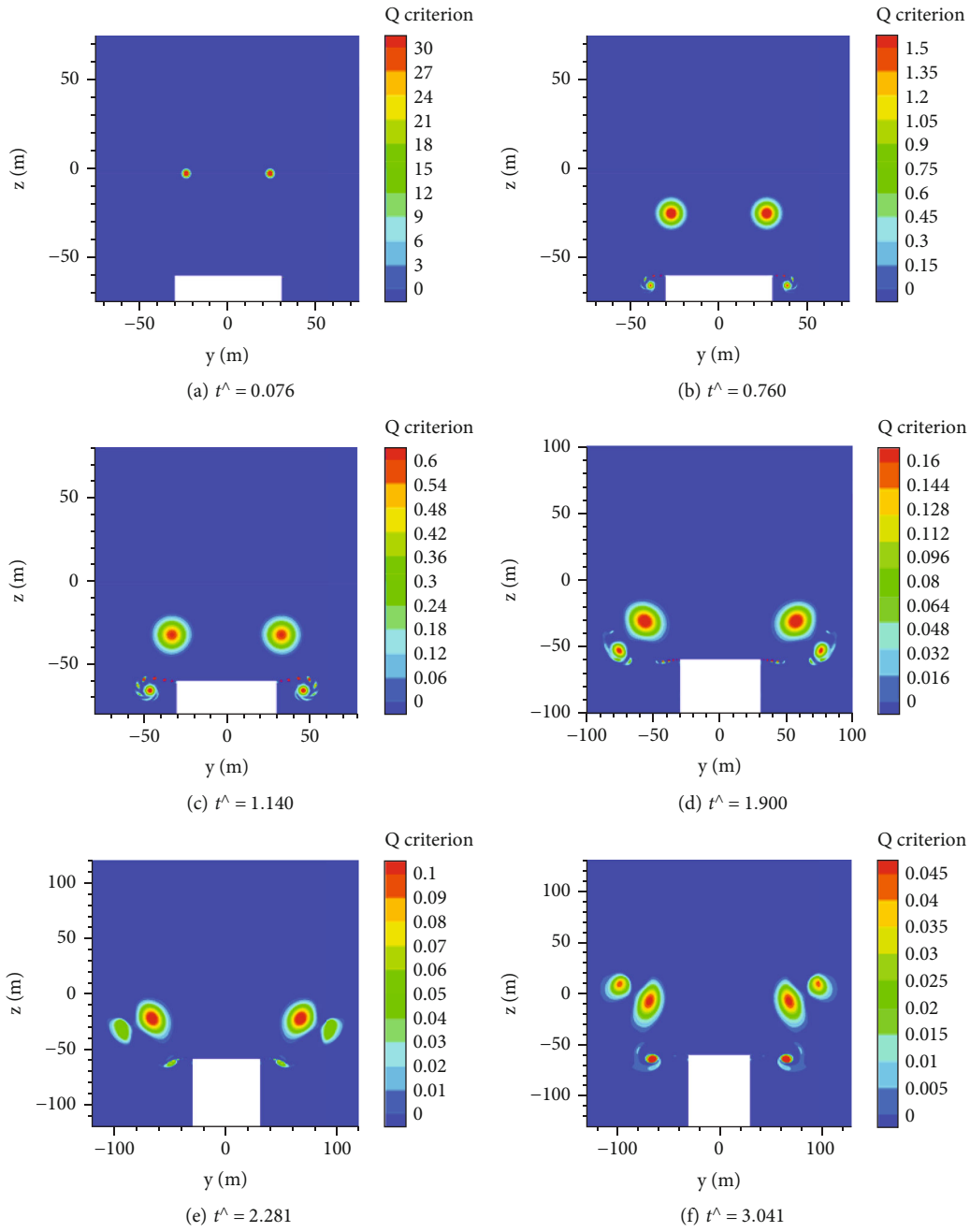


Figure 17: Contours of $Q$ criterion at different times when the wake is 60 m above the obstacle.

of the obstacle and rotate in the opposite direction to the rotation direction of the wake vortex. In addition, at $t^{\wedge} = 3.014$, secondary vortex is also generated between the two vortices.

Wake vortex core spacing and wake vortex height also changed. Affected by obstacle and secondary vortex, after $t^{\wedge} = 1.900$, the wake vortex high increase first followed by decrease when the wake vortex core spacing increases rapidly. Then, the secondary vortex rotates and gradually merged to a larger secondary vortex. Due to the different rotation directions of the secondary vortex and the wake vortex, the wake vortex intensity will decrease rapidly at this stage, and its shape becomes flat and irregular.

Figures 16 and 17 are the contours of the wake vortex velocity and the $Q$ criterion when the wake is 60 m above the obstacle. Compared with the situation when the wake is 100 m above the obstacle, before $t^{\wedge} = 2.281$, there is no difference in the change of the wake vortex structure. Multiple secondary vortices will be generated on both sides of the obstacle and eventually merge into one secondary vortex. After $t^{\wedge} = 2.281$, we found that new secondary vortices were generated at both ends of the obstacle. The new secondary vortex rotates in a different direction than the wake vortex and starts to revolve around the main vortex along the trajectory of the original secondary vortex. The previously

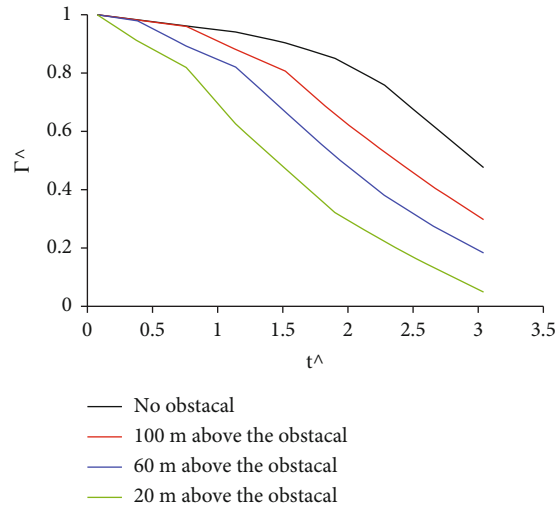


Figure 18: Variation of circulation.

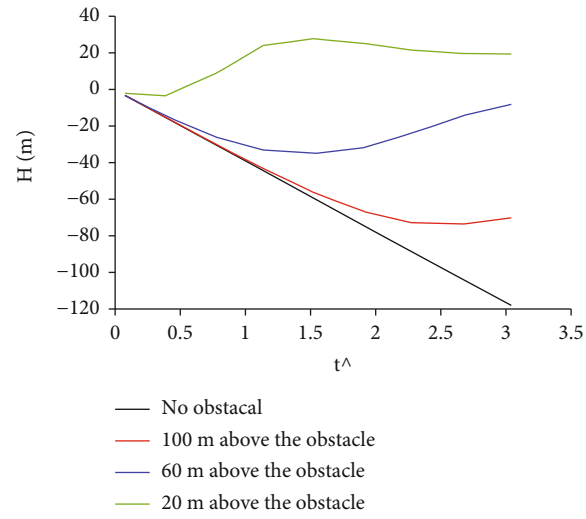


Figure 19: Variation of wake vortex height.

generated secondary vortex begins to revolve around the wake vortex and begins to merge into the wake vortex.

Contours of $Q$ criterion and velocity when the wake is 100 m above the obstacle are similar to those of 60 m above the obstacle. Therefore, we give the conclusion for it is 100 m above the obstacle. We found that before $t^{\wedge} = 0.760$, the wake vortex structure changes the same as the previous case. After this time, the initially generated secondary vortex revolved around the wake vortex and merged into wake vortex, and the later generated secondary vortex also revolved around the main vortex and gradually merged with the main vortex. We found that more and more secondary vortices are generated near the primary vortex, which leads to a faster decay of the wake vortex intensity and an increasingly irregular wake vortex structure. At the same time, under the influence of obstacle and secondary vortices, wake vortex core spacing also increases rapidly, while wake vortex height does not increase further, which is significantly different from the wake vortex under the influence of ground effect.

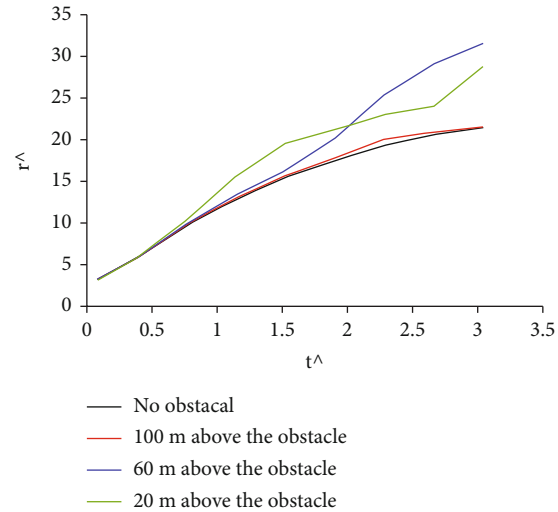


Figure 20: Variation of wake vortex core radius.

We also obtained quantitative data on the variation of wake vortex intensity and position under different conditions. Figure 18 shows the results of circulation. It can be seen from the results that when the wake is 20 m above the obstacle, its circulation decay speed is the fastest. The decay speed is the slowest when there is no obstacle. This result is also in line with the actual and expected. We found that when there is an obstacle, the variation law of the wake vortex circulation is relatively similar. At the initial moment of the decay stage, the decay rate of the circulation is small, and then, the circulation enters a period of rapid decay. What we can make clear is that the presence of obstacles accelerates the time when the circulation enters a fast decay phase. And the closer the wake vortex is to the obstacle, the faster the circulation will enter fast decay phase. The two-stage decay of the circulation is consistent with the relevant theory of the wake vortex intensity dissipation. From the analysis of the wake vortex structure in the previous section, it can be seen that when there is an obstacle, the time when the circulation enters the rapid decay is exactly the time when the secondary vortex generated and interacts with the wake vortex.

Figure 19 is the variation result of wake vortex height. Under the condition of no obstacle, the height of the wake vortex decreases linearly, which is consistent with the content in Section 3.2. When there is an obstacle, the influence law of the obstacle on the wake vortex height is basically the same. Obstacle causes a rise in wake vortex height. The smaller the distance the wake is above the obstacle, the faster the wake vortex height rise will occur. However, the obstacle will not cause the height of the wake vortex to continue to rise, such as the case of 20 m above the obstacle. This is mainly because, first of all, the wake vortex itself has a downward trend. Then, the influence of the secondary vortex on the wake vortex height is also changing. We found that when the secondary vortex is on the left side of the left wake vortex, the rotation will cause the height of the wake vortex to rise, and when it is on the right side of the left wake vortex, it will cause the wake vortex to decrease.

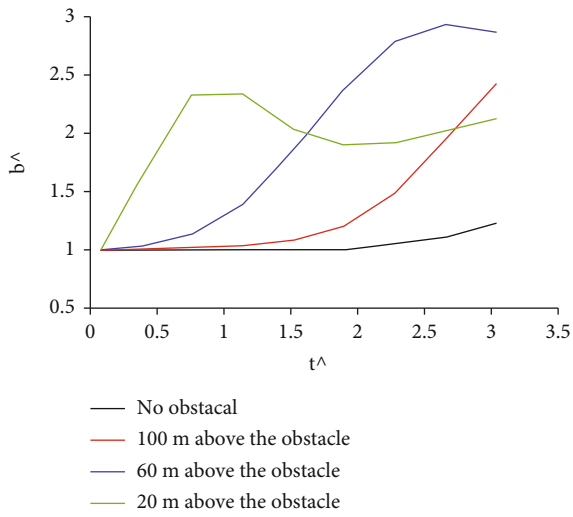


Figure 21: Variation of wake vortex core spacing.

Figure 20 is the variation result of wake vortex core radius. It can be seen that the radius of the vortex core continues to increase, and the existence of obstacle will lead to a further increase in the wake vortex core radius. In our calculation time, the results are the same when the wake is 100 m above the obstacle and when there is no obstacle. This is because the influence of the obstacle on the wake vortex occurs in the last stage when the wake is 100 m above the obstacle, so its influence on the wake vortex core radius is limited. In the other two cases, the obstacle has a greater influence on the wake vortex, which leads to the increase of the wake vortex core radius.

Figure 21 is the calculation result of the wake vortex core spacing. We found that the distance between vortex cores will increase because of turbulence and the interaction of left and right vortices, and obstacle will further increase the distance between vortex cores. This can also be seen from the previous $Q$ criterion contours. This is mainly due to the effect of secondary vortices. When the secondary vortex is generated, its rotation direction is opposite to that of the wake vortex, so the secondary vortices will make the wake vortex move to the outside. However, as the intensity of the secondary vortex decreases and the secondary vortex on the left and right side of the wake vortex will cause the wake vortex to shift to different directions, the increase in wake vortex core spacing is limited.

## 4. Conclusion

The law of the influence of a single obstacle on the intensity, structure, and position of the wake vortex is different from the ground effect situation of previous studies. A single obstacle can accelerate the decay rate of the circulation; this is because it leads to the generation of the secondary vortices, and the secondary vortices accelerate the decay rate of the circulation. This principle is similar to the principle that a plate-line device accelerates the decay rate of the circulation which is studied by DLR. We also found that single obstacle causes the circulation to decay at different rates at different stages. When multiple secondary vortices are generated and merged into a larger secondary vortex, the decay rate of the circulation is the fastest, and when the vortex core spacing increases and the intensity of the secondary vortex decreases, the decay rate of the circulation decreases compared to the fastest decay rate. The distance of the wake vortex above the obstacle directly affects the decay rate and the time for the wake vortex to enter the fast decay phase.

The influence of a single obstacle on the structure and position of the wake vortex is also different. The wake vortex becomes flat and irregular under the influence of obstacle and secondary vortices. This is due to the direct blocking effect of the obstacle on the wake vortex, and the formed secondary vortex revolves around the wake vortex and merges into the wake vortex. Compared with no obstacle, wake vortex core radius and wake vortex core spacing will increase when there is a single obstacle. The increase of wake vortex core spacing is mainly due to the effect of the secondary vortices generated between the left and right vortices. However, wake vortex core spacing will not increase all the time, because the secondary vortex generated on both sides of the obstacle rotates around the wake vortex that causes the wake vortex core spacing increased and then fluctuates around this space value. Wake vortex core radius is larger when there is obstacle than when there are no obstacles. On the one hand, it is because the increase of wake vortex core spacing, the interaction between the left and right vortices decreases, on the other hand, because of the interaction between the secondary vortex and the wake vortex. Wake vortex height is also affected by obstacle. Wake vortex height decreases linearly without obstacles, while wake vortex height increases when there is an obstacle. However, when there is obstacle, wake vortex height does not always increase; instead, after rising to a value, it fluctuates around this value. This is also caused by the secondary vortex revolving around the wake vortex.

## Abbreviations

LES: Large eddy simulation
$\rho$: Density
t: Time
$\bar{u}$: Mean speed
$\bar{p}$: Mean pressure
$\mu$: Fluid viscosity coefficient
$\delta_{ij}$: Subgrid-scale strain rate
$\tau_{ij}$: Subgrid-scale stress
$\overline{h_s}$: Mean sensible enthalpy
$\lambda$: Thermal conductivity
$\overline{S_{ij}}$: Rate-of-strain tensor
k: von Karman constant
d: Distance to the closest wall
$V$: Volume of a computational cell
$\bar{T}$: Mean temperature
$\mu_{SGS}$: Subgrid viscosity
$Pr_{SGS}$: Subgrid Prandtl number
$C_p$: Specific heat
$\tau_{kk}$: Isotropic part of the subgrid-scale stresses

$\mu_t$: Subgrid-scale turbulent viscosity
$L_s$: Mixing length for subgrid scales
$S_{ij}$: Strain rate tensor.

*Units of Measurement*

| | |
|---|---|
| Meter (m): | Distance, height |
| Second (s): | Time |
| Meters per second (m/s): | Speed |
| Degree (°): | Angle |
| Kelvin (K): | Temperature |
| Kilogram/cubic meter ($kg/m^3$): | Density |
| Newton (N): | Pressure |
| One per second (1/s): | Vorticity |
| One per second squared ($s^{-2}$): | $Q$ criterion |
| One per second squared ($s^{-2}$): | Lambda 2 criterion. |

## Data Availability

The data used to support the findings of this study are available from the corresponding author upon request.

## Conflicts of Interest

The authors declare that there is no conflict of interest regarding the publication of this article.

## Acknowledgments

The study is supported by the National Natural Science Foundation of China (U1733203) and Civil Aviation Professional Project (TM2019-16-1/3).

## References

[1] F. Barbaresco, P. Juge, M. Klein, Y. Ricci, J. Y. Schneider, and J. F. Moneuse, "Optimising runway throughput through wake vortex detection, prediction and decision support tools," in *2011 Tyrrhenian International Workshop on Digital Communications - Enhanced Surveillance of Aircraft and Vehicles*, Capri, 2011.

[2] C. Schwarz and K. U. Hahn, "Impact of individual and dynamic wake vortex separations on airport capacity," in *Conference Proceedings ICAS 2006*, Hamburg, Germany, 2006.

[3] Wake turbulence event Sydney airport, *An aviation occurence investigation report of the Australian Transport Safety Bureau*, DLR, 2008.

[4] Summary Report, *XB-70 Accident Investigation*, USAF, 1966.

[5] S. C. Crow, "Stability theory for a pair of trailing vortices," *AIAA Journal*, vol. 8, no. 12, pp. 2172–2179, 1969.

[6] G. C. Greene, "An approximate model of vortex decay in the atmosphere," *Journal of Aircraft*, vol. 23, no. 7, pp. 566–573, 1986.

[7] A. Corjon and T. Poinsot, "Vortex model to define safe aircraft separation distances," *Journal of Aircraft*, vol. 33, no. 3, pp. 547–553, 1996.

[8] T. Sarpkaya, "New model for vortex decay in the atmosphere," *Journal of Aircraft*, vol. 37, no. 1, pp. 53–61, 2000.

[9] F. Holzäpfel, "Probabilistic two-phase wake vortex decay and transport model," *Journal of Aircraft*, vol. 40, no. 2, pp. 323–331, 2003.

[10] F. Holzäpfel, T. Gerz, and E. Stumpf, "Strategies for circulation evaluation of aircraft wake vortices measured by lidar," *Journal of Atmospheric and Oceanic Technology*, vol. 20, no. 8, pp. 1183–1195, 2003.

[11] T. Louagie, L. Georges, and P. Geuzaine, "Numerical simulation of wake vortex flows: RANS-LES of a fuselage wake and LES of wake vortices in ground effect with and without wind," in *43rd Conference on Applied Aerodynamics*, Poitiers, France, 2008.

[12] A. Stephan, F. Holzäpfel, and T. Misaka, "Aircraft wake-vortex decay in ground proximity—physical mechanisms and artificial enhancement," *Journal of Aircraft*, vol. 50, no. 4, pp. 1250–1260, 2013.

[13] L. Nybelen and R. Paoli, "Direct and large-eddy simulations of merging in corotating vortex system," *AIAA Journal*, vol. 47, no. 1, pp. 157–167, 2009.

[14] T. Misaka, F. Holzapfel, and T. Gerz, "Wake evolution of high-lift configuration from roll-up to vortex decay," in *AIAA Aerospace Sciences Meeting Including the New Horizons Forum and Aerospace exposition*, pp. 1–11, Grapevine (Dallas/Ft. Worth Region), Texas, 2013.

[15] F. N. Holzäpfel, A. Stephan, and T. Misaka, "Wake vortex evolution during approach and landing with and without plate lines," in *Aerospace Sciences Meeting*, pp. 405–417, National Harbor, Maryland, 2014.

[16] F. N. Holzäpfel, A. Stephan, N. Tchipev, T. Heel, S. Körner, and T. Misaka, "Impact of wind and obstacles on wake vortex evolution in ground proximity," in *6th AIAA Atmospheric and Space Environments Conference*, p. 2470, Atlanta, GA, 2014.

[17] T. A. Stuart, X. Mao, and L. Gan, "Transient growth associated with secondary vortices in ground vortex interactions," *AIAA Journal*, vol. 54, no. 6, pp. 1901–1906, 2016.

[18] S. Paramasivam, D. Zhao, and M. Skote, "Detailed study of effects of crosswind and turbulence intensity on aircraft wake vortex in ground proximity," in *34th AIAA Applied Aerodynamics Conference*, p. 4184, Washington, D.C., 2016.

[19] T. Misaka and S. Obayashi, "Numerical study on jet-wake vortex interaction of aircraft configuration," *Aerospace Science and Technology*, vol. 70, pp. 615–625, 2017.

[20] Y. X. Zhang and F. X. Wang, "Multi-stage evolution process of wingtip vortex and its influence on aerodynamic force," *Science Technology and Engineering*, vol. 16, no. 19, pp. 11–19, 2016.

[21] M. D. Lin, G. X. Cui, and Z. S. Zhang, "Large eddy simulation study on aircraft wake vortex evolution and rapid development dynamic prediction," *Chinese Journal of Theoretical and Applied Mechanics*, vol. 49, no. 6, pp. 1185–1200, 2017.

[22] J. X. Zhou, C. Y. Chen, D. Li, Z. Y. Zhang, and W. J. Pan, "Numerical simulation of aircraft wake vortex evolution and wake encounters based on adaptive mesh method," *Engineering Applications of Computational Fluid Mechanics*, vol. 14, no. 1, pp. 1445–1457, 2020.

[23] D. Li, Z. M. Xu, K. Zhang et al., "Study on the influence of linear and nonlinear distribution of crosswind on the motion of aircraft wake vortex," *Proceedings of the Institution of Mechanical Engineers, Part G: Journal of Aerospace Engineering*, vol. 235, no. 14, pp. 1981–1990, 2021.